Nano Energy 67 (2020) 104211

Contents lists available at ScienceDirect

Nano Energy

journal homepage: http://www.elsevier.com/locate/nanoen

Review

Electroactivation-induced spinel ZnV_2O_4 as a high-performance cathode material for aqueous zinc-ion battery

Yi Liu, Chang Li, Jia Xu, Mingyang Ou, Chun Fang **, Shixiong Sun, Yuegang Qiu, Jian Peng, Gongchang Lu, Qing Li, Jiantao Han *, Yunhui Huang

State Key Laboratory of Material Processing and Die & Mould Technology, School of Materials Science and Engineering, Huazhong University of Science and Technology, Wuhan, 430074, PR China

ARTICLE INFO

Keywords:
Aqueous zinc-ion battery
Spinel cathode
Electrochemically activation
Zinc storage mechanism

ABSTRACT

Rechargeable and affordable aqueous zinc-ion batteries (ZIBs) with high energy density are needed for large-scale energy storage systems. However, the development of ZIBs has stagnated due to the lack of stable high-capacity cathode materials. Here, a typical spinel ZnV_2O_4 has been investigated as a ZIB cathode, and a significant electroactivation reaction was observed during the initial electrochemical cycles. After electroactivation, ZnV_2O_4 exhibits a high reversible capacity of 312 mAh g^{-1} and retains a capacity of 206 mAh g^{-1} over 1000 cycles at a high rate of 10 C. The electroactivation process was then analyzed via *in-situ* XRD, *ex-situ* PDF, *ex-situ* HADDF-STEM, *ex-situ* XPS, and various electrochemical measurements. The electroactivation enhances the surface electrochemical reaction with self-adaptive adjustment of the lattice structure. This guarantees outstanding electrochemical performance. The encouraging results deepen our understanding of rechargeable aqueous batteries and offer insight into the design of high-performance electrode materials for rechargeable aqueous ZIBs.

1. Introduction

Large-scale energy storage technologies are critical for the integration of amounts of distributed renewable energy and power infrastructures to improve grid reliability and utilization [1,2]. Although lithium-ion battery technologies continue to mature, their application in grid-scale energy storage has still been limited due to cost and safety concerns [3,4]. Low-cost and high-safety aqueous rechargeable batteries with earth-abundant, inexpensive materials as charge carriers are a promising alternative [5,6]. The low redox potential of Zn/Zn^{2+} (−0.76 V versus standard hydrogen electrode (SHE)) combined with a two-electron-transfer electrochemical reaction is a high energy density electrochemical system—especially for aqueous zinc-ion batteries (ZIBs) [6–9]. However, the reported cathode materials for aqueous ZIBs face various challenges: Prussian blue analogs with stable structures are constrained by low capacity [10,11], while high capacity manganese-based oxides suffer from drastic capacity fading due to irreversible structural changes caused by Mn^{2+} dissolution [12,13].

Due to the low-cost (~US $7.85/lb) and stable open framework of vanadium oxides—as well as the stable long-cycle life and high specific capacity—vanadium-based materials have been intensively studied as electrode materials in aqueous ZIBs [14,15]. Among various vanadium-based materials, layered vanadium oxides have attracted much attention. Due to their tunable layer spacing, layered vanadium oxides are often described as ideal hosts for various metal-ions [16,17]. Ever since layered $Zn_{0.25}V_2O_5$ was reported as a high-performance cathode for aqueous ZIBs [7] by Nazar and her colleagues, additional layered structural materials have been described including LiV_2O_5 [18], NaV_3O_8 [19], $Ca_{0.25}V_2O_5$ [20]. These all apply the same strategy of pre-intercalated metal-ions in the interlayers of vanadium oxides to store free-moving ions in aqueous batteries. Meanwhile, various tunnel-type vanadium-based compounds (VO_2 [21], $LiV_2(PO_4)_3$ [22], and $Zn_3V_2O_7(OH)_2$ [23]) have also been reported as potential candidate electrode materials for aqueous ZIBs. However, these previous reports mainly attributed their electrochemical energy storage performance to the diversity of vanadium oxidation states and suitable open-framework structures. Spinel cathodes have good application in various aqueous batteries and benefit from the stable tunnel structure [24,25]. Here, a

* Corresponding author.
** Corresponding author.
E-mail addresses: fangchun@hust.edu.cn (C. Fang), jthan@hust.edu.cn (J. Han).

https://doi.org/10.1016/j.nanoen.2019.104211
Received 8 September 2019; Received in revised form 7 October 2019; Accepted 18 October 2019
Available online 22 October 2019
2211-2855/© 2019 Published by Elsevier Ltd.

typical spinel ZnV_2O_4 was first investigated as a high-performance cathode material for aqueous ZIBs although its crystallographic structure has been reported over the past few decades [26–28].

In this study, we demonstrate spinel ZnV_2O_4 as a stable high-capacity cathode material for aqueous ZIBs. Electrochemical measurements show that the spinel ZnV_2O_4 undergoes a significant electroactivation process during the initial electrochemical cycles. After electroactivation, the cathode material exhibits an extremely high reversible capacity of 312 mAh g^{-1} and retains capacity of 206 mAh g^{-1} over 1000 cycles at a high rate of 10 C. The electroactivation process and electrochemical reaction mechanism of spinel ZnV_2O_4 electrodes have been investigated systematically. The results suggest that electroactivation-induced spinel ZnV_2O_4 has high capacity and excellent cyclic stability, which is advantageous for cathodes in aqueous ZIBs.

2. Result and discussion

2.1. Structure and morphology analysis

X-ray diffraction (XRD) analyzed the lattice structure. The XRD pattern of the obtained ZnV_2O_4 powder with Rietveld refinements is represented in Fig. 1b. The Bragg reflection peaks are readily indexed in the $Fd\bar{3}m$ cubic space group. The refined profile agrees well with the experimental data indicating the formation of standard face-centered cubic spinel structure (Fig. 1a). The scanning electron microscopy (SEM) image of ZnV_2O_4 powder (Fig. S1) reveals a nanoparticle morphology, and the corresponding energy dispersive X-ray spectroscopy (EDX) elemental mapping indicates that the Zn, V, and O elements are homogeneously distributed.

The transmission electron microscopy (TEM) image (Fig. 1c) further shows that the nanograins are uniformly distributed and separated with a diameter of 30–100 nm. Meanwhile, the high-magnification TEM image in Fig. 1d reveals lattice fringes with a *d*-spacing of 0.296 nm corresponding to a (022) face. The *d*-spacing values calculated from the inserted selected area electron diffraction (SAED) are 0.146, 0.241, and 0.296 nm, which reflect the (044), (222), and (022) diffraction rings of spinel ZnV_2O_4, respectively.

As a broadly insightful characterization tool to probe local atomic structure, atomic pair distribution function (PDF) provides local structural information for nanoparticles. Here, PDF analysis gives atomic-scale insight into the crystal structure of ZnV_2O_4. Well-defined peaks in the PDF profile are related to atom-atom distances and bond lengths, and the spatial extent of peaks within the PDF directly corresponds to the ordered structure over the length scale [29,30]. The obtained PDF profile nicely fits with the crystallographic structure model of ZnV_2O_4 derived from the Rietveld refinement at the range of 0–50 Å (Fig. S2). Fig. 2 gives a direct view of the assignment of the significant peaks within the PDF corresponding to the bond lengths and atom-atom distances among Zn, V, and O atom from 0 to 10 Å.

2.2. Electrochemical performance of the ZnV_2O_4 electrode

The electrochemical performances of spinel ZnV_2O_4 cathode was investigated with a CR2032 type coin cells that uses metallic zinc as the anode and 2 M $Zn(ClO_4)_2$ aqueous solution as the electrolyte. Fig. 3a displays the cyclic voltammetry (CV) curves of the 1st and 10th cycle. In the first cycle, there are two anodic peaks at 1.12 and 0.80 V (vs. Zn/Zn^{2+}) and only one cathodic peak at 0.58 V (vs. Zn/Zn^{2+}). Interestingly, with the electrochemical reaction undergoing 10 cycles, the sharp oxidation peak at 1.12 V broadens while a new reduction peak appears at 0.94 V indicating that a new redox reaction process occurs.

Furthermore, the electrochemically active area of the 10th cycle in the CV curve is nearly 1.5 times larger than that of the 1st cycle. The increasing active area of the CV curve means an increase of the total

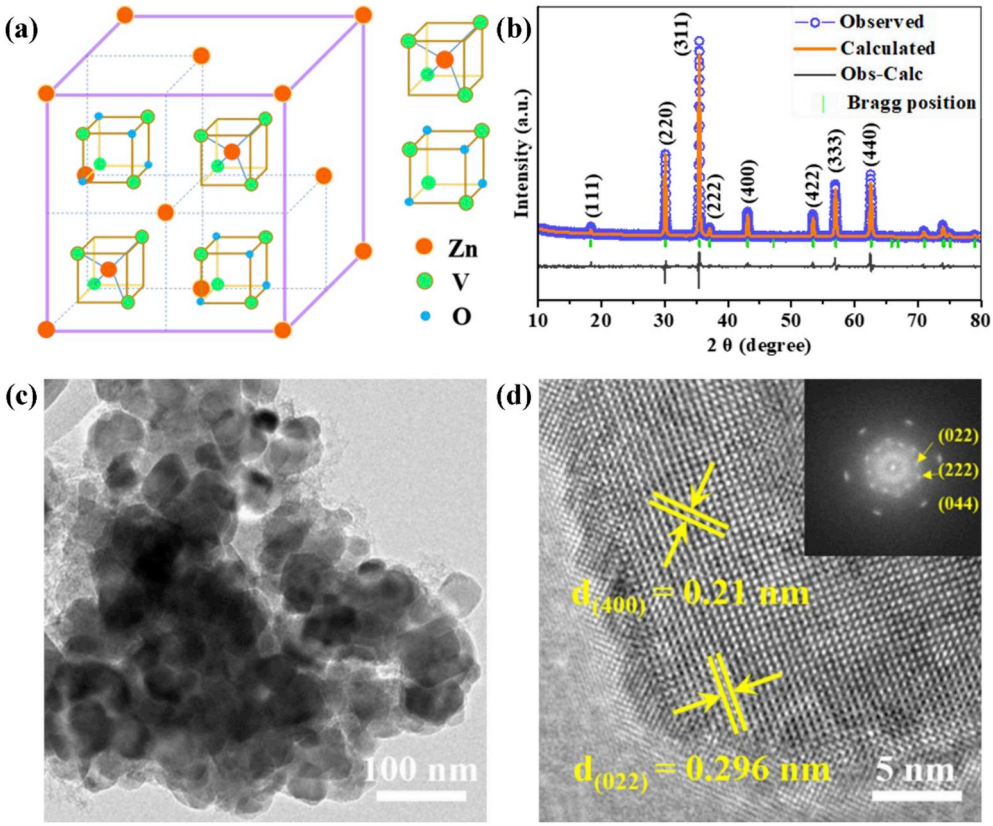


Fig. 1. a) Crystal structure of the spinel ZnV_2O_4. b) XRD pattern of the ZnV_2O_4 powder and its Rietveld refinement result. c) TEM image. d) High-magnification TEM image with SAED patterns.

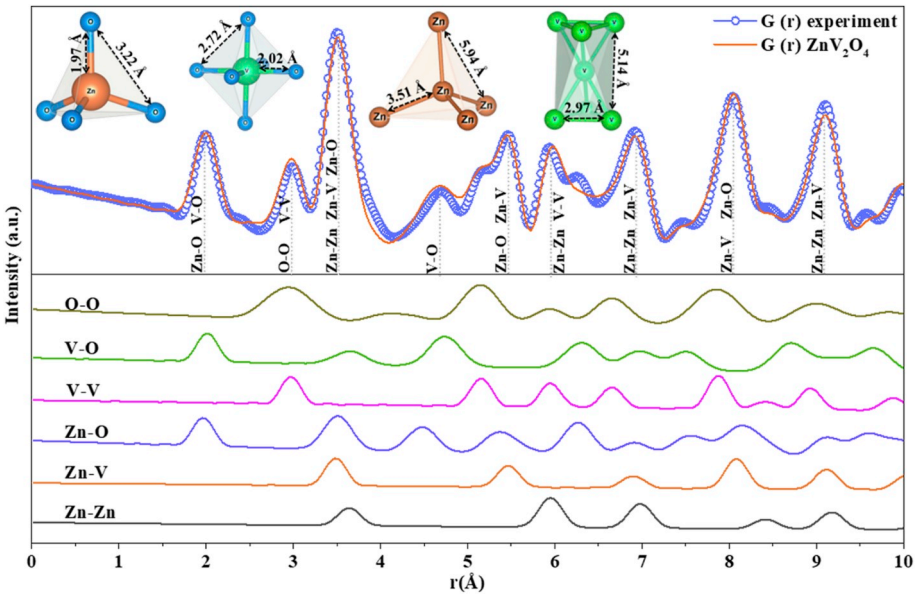


Fig. 2. The refinement of PDF in the model of cubic phase of spinel ZnV_2O_4 and the main assignment of the PDF peaks from 0 to 10 Å.

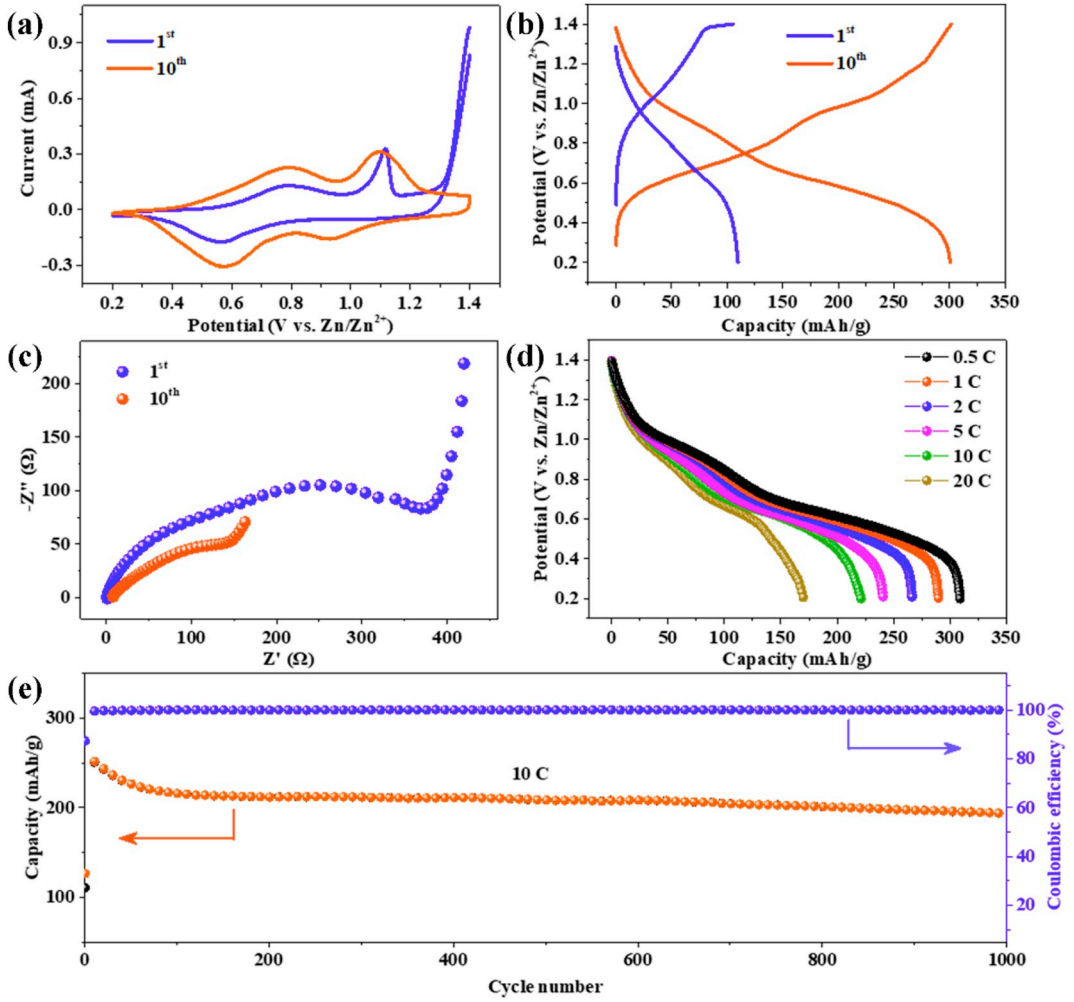


Fig. 3. Electrochemical behavior of Zn/ZnV_2O_4 batteries with 2-M $Zn(ClO_4)_2$ as electrolyte. a) CV curves in the first and 10th cycle. b) Charge–discharge curves in the first and 10th cycle. c) EIS curves in the first and 10th cycle. d) Discharge profiles at varying C rates. e) Long-term cyclic performance.

electrochemical capacity. The comparison of the curve profile is plotted in Fig. 3b. The changes in the CV curves and the charge/discharge profiles suggest that there would be an electroactivation process during the initial cycles. The greatly reduced electrochemical impedance (Fig. 3c) also reveals a faster charge transfer kinetic occurred after electroactivation, which agrees well with the CV and charge/discharge curves. The rate capability of the Zn/ZnV_2O_4 cells cycling in the voltage range of 0.2–1.4 V (vs. Zn/Zn^{2+}) is shown in Fig. 3d with average discharge capacities of 312, 289, 271, 244, 222 and 174 mAh g^{-1} at a rate of 0.5, 1, 2, 5, 10, and 20 C, respectively. The Zn/ZnV_2O_4 cells are discharged/charged at 10 C to evaluate the long-cycle stability. Remarkably, the cycling performance shows that the initial discharge capacity is 117 mAh g^{-1}; the capacity rapidly increases to 252 mAh g^{-1} in the initial few cycles, which could be attributed to the gradual electroactivation of the active material (Fig. 3e). Importantly, the reversible capacity retains at 206 mAh g^{-1} over 1000 cycles with a Coulombic efficiency approaching 100%.

2.3. Electrochemical mechanisms

Vanadium oxides usually exhibit good surface capacitive effects induced by the multiple redox reactions of vanadium-ions at the interface between the electrode and electrolyte [31]. To clarify the capacitive and diffusion-controlled effects, we investigated the electrochemical kinetics of the ZnV_2O_4 electrode in detail. Fig. 4a shows CV profiles with similar shapes at various scan rates from 0.2 to 1 mV/s. These profiles display two couples of broad cathodic and anodic peaks with increasing scan rates. The peak currents (i) usually obeys a formula with the scan rate (v) as [32] $i = av^b$; here, b can be calculated by the slope of the log(i) vs. log(v) plots. Generally, the coefficient b varies in the range between 0.5 and 1.0 while the b-value of 0.5 and 1.0 represents diffusion-controlled and capacitive effects, respectively. The b values are 0.76 and 0.74 during the discharging process, respectively, based on the peak current of the activated ZnV_2O_4 electrodes (Fig. 4b). The results indicate that the capacitance effect dominates in the electrochemical process.

Additionally, the capacitive contribution ratio can be further quantified by separating the response current at a fixed potential into capacitive effects and diffusion-controlled reactions. The equation can be described as below [33]:

$$i(V) = k_1 v + k_2 v^{1/2}$$

Here, $k_1 v$ corresponds to the capacitive effects while $k_2 v^{1/2}$ represents the diffusion-controlled effects. By determining k_1 and k_2, the calculated capacitance ratios at various scan rates are exhibited in Fig. 4c. The consequences indicate that the capacitive effects play an essential role in the capacity and the capacitive contribution increases gradually with the increasing scan rate.

Next, the galvanostatic intermittent titration technique (GITT) measurement was used in which current pulses (0.1 A g^{-1}) of equal duration (10 min) were applied followed by 20 min' relaxation for each current pulse. This GITT experiment further investigated the electrochemical reaction kinetics of Zn^{2+} diffusion during electrochemical cycling. The charge/discharge curves and calculated diffusion coefficients of Zn^{2+} for activated ZnV_2O_4 are presented in Fig. 4d. For the (de-)insertion process, the apparent diffusion coefficient of Zn^{2+} undergoes two fluctuations that correspond to two oxidation/reduction process. Moreover, the average D_{Zn} value in ZnV_2O_4 is calculated to be about $7*10^{-10}$ cm^2 s^{-1}, which is superior to the diffusion coefficient of Zn^{2+} in spinel $ZnMn_2O_4$ [24]. The Nyquist plots in Fig. 3c also demonstrate that the activated ZnV_2O_4 exhibits fast ionic diffusion as well as excellent charge transfer kinetics that are favorable for fast energy storage and conversion.

To determine the electroactivation mechanism, *in situ* XRD was performed to investigate the structural evolutions during the initial two galvanostatic charge–discharge cycles. Fig. 5a shows a 2D contour map of the *in situ* XRD pattern. This pattern shows that the (111) peak maintains the same position and intensity throughout the entire electrochemical process while the (220) and (331) peaks of ZnV_2O_4 decrease gradually in the first charge process. This proceeds until the second cycle

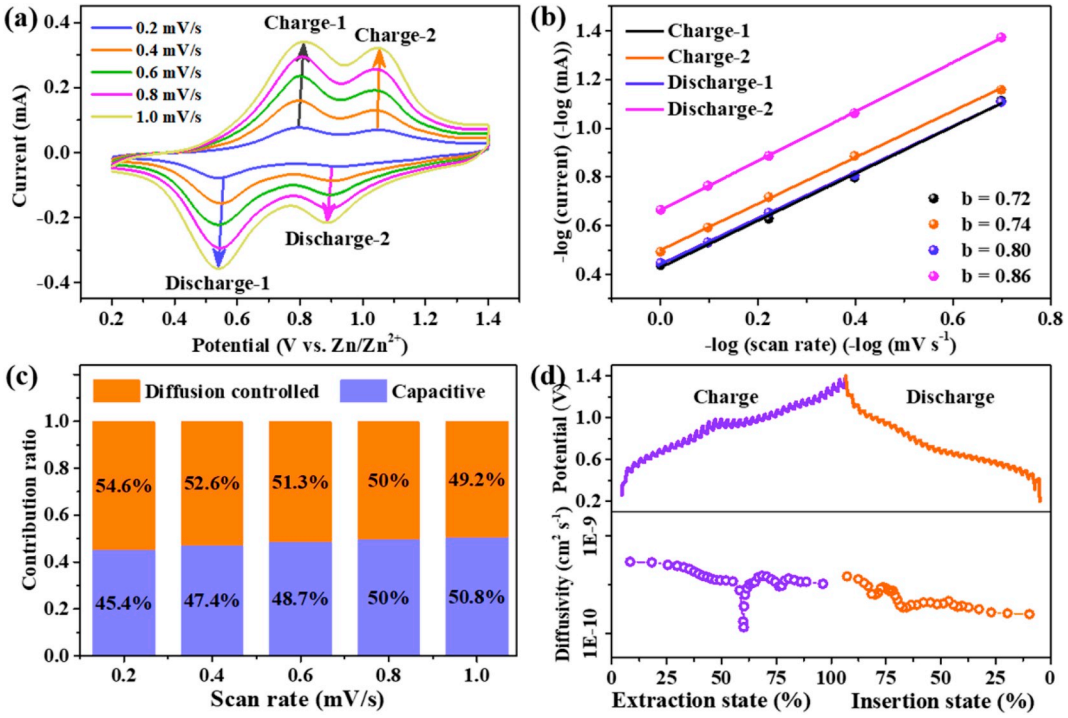


Fig. 4. Electrochemical performances of the activated Zn/ZnV_2O_4 batteries cycling in a range of 0.2–1.4 V. a) CV curves at different scan rates. b) Log (current) vs. log (scan rate) plots of four peaks in the CV curves during cycling. c) The contribution ratio of the capacitive capacities and diffusion-limited capacities. d) GITT profiles and calculated Zn^{2+} diffusion coefficient.

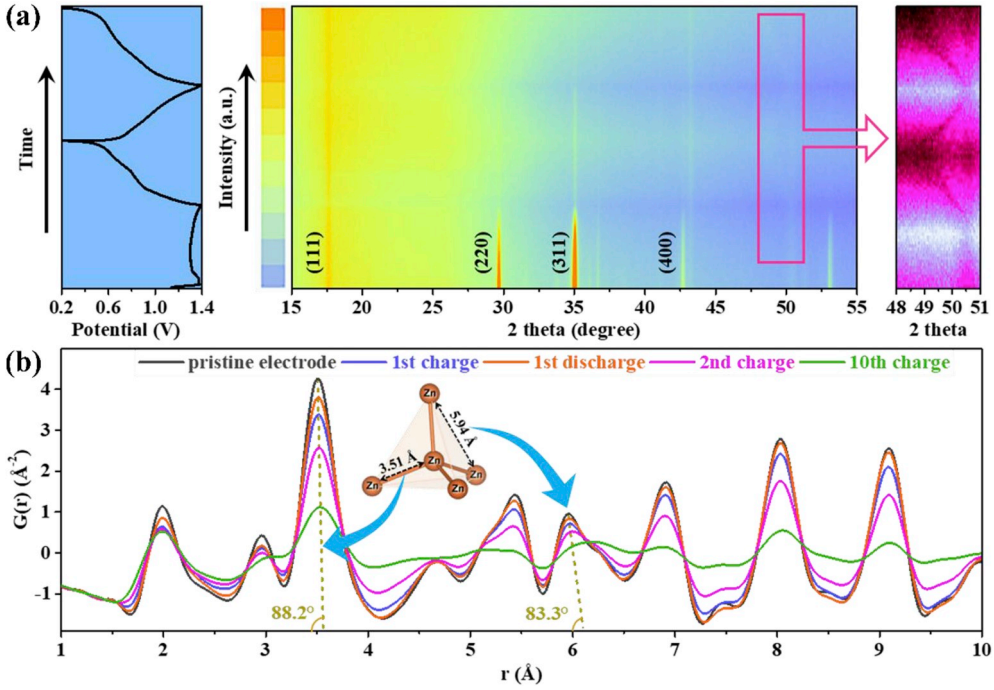


Fig. 5. a) *In situ* XRD measurement of the ZnV_2O_4 electrode during the first two cycles. b) *Ex situ* PDF analysis of the ZnV_2O_4 electrode from 0 to 10 Å.

the intensity of the peaks decreases by nearly 95%, which indicates a micro-crystallization process of ZnV_2O_4. The peak at 43.1° is due to the stainless-steel mesh current collector. Interestingly, a very weak peak appears at 50.5° during the initial charge process. The variations of XRD patterns suggest the emergence of a new Zn-poor $Zn_xV_2O_4$ phase due to the extraction of Zn^{2+}. Upon discharge, the magnified XRD peak at 50.5° shifts to 48.7°, which could be related to the simultaneous intercalation of Zn^{2+} into the tunnels parallel. The shift of the principal peak also reveals the lattice expansion at the Zn^{2+} insertion state. When discharging from 1.4 to 0.2 V, the peak shifts reversibly to the original location and retains cyclical fluctuation in the next galvanostatic charge-discharge cycle indicating good reversibility of Zn^{2+} (de-)insertion in activated ZnV_2O_4. The new reversible peak also agrees well with the emergence of the second CV redox peaks around 0.94 V. The structural evolutions occasionally accompanying metal ion (de)insertion are so complex that the XRD pattern is difficult to interpret with no direct demonstration of the structural evolution trend [34].

Ex situ PDF analysis (Fig. 5b) leads to atomic-scale insight into the structural evolution process of spinel ZnV_2O_4 during the galvanostatic charge–discharge cycles. The overall intensity of the curve decreases gradually as the electrochemical cycle continues, which indicates a decrease in particle size. The size of the particle or coherent domain dominates the intensity of the PDF peaks [35–37]; thus, the phenomenon that the peaks converge at much smaller *r* value further confirms the micro-crystallization process (Fig. S3). Compared with the 1st charge state (blue line), the intensity of the peaks at the 1st discharge state (orange line) is higher due to the Zn^{2+} insertion. The intensity of these peaks is much lower until the 2nd charge state (pink line). This regular fluctuation demonstrates a Zn^{2+} (de-)insertion process. Fig. 5b shows that there is a positive shift of the peaks at 3.51 Å and 5.94 Å, which corresponds to Zn–Zn, Zn–V, and Zn–O, indicating that lattice distortion appears. This can be attributed to the adaptive adjustment of lattice structure accompanying Zn^{2+} migration [38]. Due to numbers of Zn^{2+} extracted from the spinel ZnV_2O_4 lattice at the charged state, the intensity of the peak at 5.94 Å decreases so much that it is incorporated into the adjacent peak to form a broader peak. However, there is no obvious shift in the position of major peaks suggesting that the lattice framework of ZnV_2O_4 remains stable during the galvanostatic charge–discharge cycles. The obvious local distortion reveals a dramatic reduction of the Zn–Zn bond ratio, which cause the lattice defects. The intensity of the peaks at 5.42 Å, 6.90 Å also has a remarkable decrease due to the reduction of the ratio of Zn–V and Zn–O bond caused by the extraction of Zn^{2+}. These results clarify the micro-crystallization process and the Zn^{2+} (de-)insertion mechanism of spinel ZnV_2O_4 at the atomic scale.

To gain further insight into the structure evolution process during the electrochemical cycle, we next investigated the *ex situ* high-angle annular dark-field scanning transmission electron microscopy (HAADF-STEM) of the electrode. Fig. 6a presents HADDF-STEM images and the corresponding EDX maps of Zn, V, and O of the ZnV_2O_4 electrode in the second charge state. A significant structural change can be observed compared with the original state of ZnV_2O_4 particles (Fig. 1c): the particles dissociate into some interconnected smaller plates. More clearly, the non-uniformity elemental distribution of Zn–V–O mapping confirms the dissociation process. The elemental content analysis of the selected zone A and B (Fig. S4) also reveals the dissociation process due to the extraction of Zn^{2+}. The inside nanopores and lattice defects further verify the beginning of the micro-crystallization process (Fig. 6b). Meanwhile, the lattice fringe with a spacing of 0.272 nm is slightly smaller than the original state upon extraction of Zn^{2+}, and the material maintains the integral frame structure.

Fig. 6c further analyzes the HADDF-STEM images of ZnV_2O_4 electrode at the 10th discharge state. A 3D interconnected network structure is presented in Fig. 6c and is believed to contribute to the enhanced electrochemical kinetics. Examining the associated EDX element maps in Fig. 6c, the bulk distribution of these elements remains uniform, and the elemental content analysis of the selected zone **C** indicates the insertion of Zn^{2+} (Fig. S4b). However, various lattice distortions can be observed in the skeleton of the network due to the reversible extraction of some zinc ions from ZnV_2O_4 (Fig. 6d). The rings seen in the SAED patterns reveal that a micro-crystallization process occurs to the active material during the electrochemical cycles, which is confirmed by the *in situ* XRD and *ex situ* PDF results. Compared with the extraction state, the lattice spacing of (222) at the insertion state increases slightly from 0.235 nm to 0.242 nm, which confirms the Zn^{2+} insertion reaction. The calculated d-spacing values are 0.139, 0.198, and 0.242 nm, which

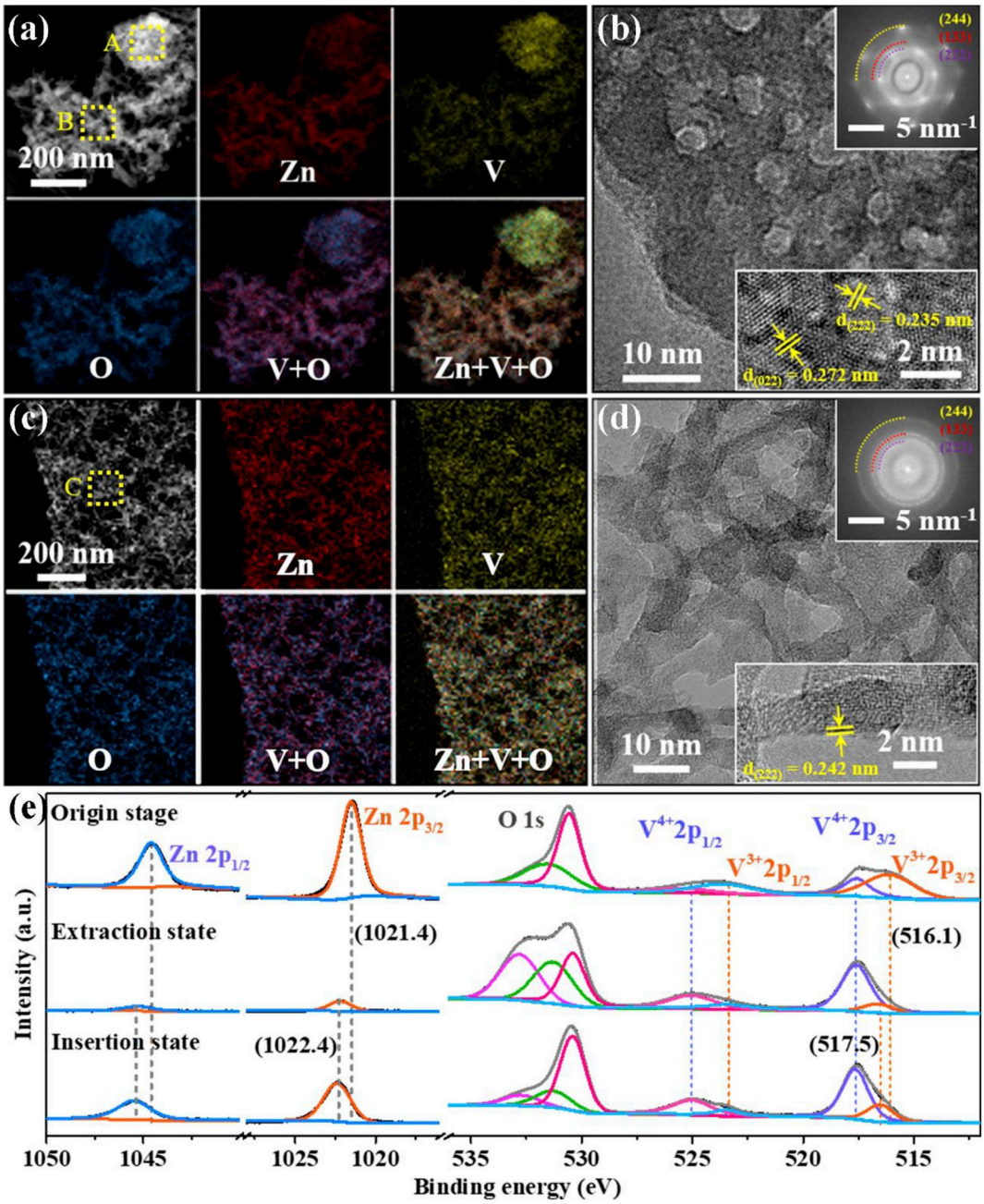


Fig. 6. *Ex situ* HADDF-STEM images: a) HADDF-STEM image with EDX-mapping of the electrode. b) High-magnification TEM image with SAED pattern at 2nd charge state. c) HADDF-STEM image with EDX-mapping of the electrode. d) High-magnification TEM image with SAED pattern at 10th discharge state. e) *Ex situ* XPS spectra of the Zn, O, and V.

reflect the (244), (133), and (222) diffraction rings of origin spinel ZnV_2O_4, respectively. The results reveal that the appropriate structural change accompanies the (de-)insertion of Zn^{2+}.

Ex situ X-ray photoelectron spectroscopy (XPS) analysis (Fig. 6e) reveals the oxidation state evolutions of zinc and vanadium during the electrochemical reaction. The pristine electrode shows only one Zn 2p component ($2p_{3/2}$: 1021.4 eV) due to the native Zn site in ZnV_2O_4. Upon extraction state, the peak of Zn 2p shifts to a higher binding energy ($2p_{3/2}$: 1022.4 eV). The distinct shift in the binding energies can be ascribed to the change in the coordination environment of zinc with oxygen and vanadium atoms in the compound. The change of bonding interactions would lead to a proper bonding rearrangement accompanying Zn^{2+} migration resulting in an excellent electrochemical performance.

The peak area of Zn 2p in the extraction state is far lower than the insertion state, which confirms the (de-)insertion of Zn^{2+}. In the original state, the V^{3+} signal ($2p_{3/2}$: 516.1 eV) accompanied by V^{4+} ($2p_{3/2}$: 517.4 eV) component reveals a mixed valence state. During charging, the extraction of Zn^{2+} results in a sharp decrease of the characteristic peak of V^{3+} while the V^{4+} peak dominates. The V^{3+} signal increases due to the Zn^{2+} insertion after discharge.

3. Conclusions

In summary, an aqueous rechargeable zinc-ion battery is assembled with a promising cathode material—an electroactivation-induced spinel ZnV_2O_4. The (de-)insertion of Zn^{2+} leads to the electroactivation process caused by the micro-crystallization of ZnV_2O_4. The electroactivation-induced ZnV_2O_4 delivers an ultra-high specific capacity of 250 mAh

g^{-1} at the high rate of 10 C with a remaining reversible capacity of 206 mAh g^{-1} after 1000 cycles. These features are due to the formation of a 3D interconnection network and self-adaptive adjustment of local lattice structure caused by the electroactivation. The aqueous ZIBs have significant potential for electrochemical energy storage because they are low-cost, safe, and eco-friendly. The development of such low-cost and high-capacity transition-metal oxides as electrode materials would certainly inspire future development of aqueous ZIBs.

4. Experimental section

4.1. Material synthesis

All chemicals and solvents were purchased from Alfa Aesar Chemical Co., Ltd. (China) and used without further purification. In a typical synthesis, $Zn(CH_3COO)_2$ (10 mmol) and NH_4VO_3 (20 mmol) were mixed with constant grinding for 0.5 h to form a precursor powder. The final spinel product was obtained by heating the precursor powder at 800 °C for 10 h in argon/hydrogen mix (containing 5% hydrogen) atmosphere.

4.2. Characterization of materials

The morphological and chemical composition characterizations were observed via a field-emission scanning electron microscope (FESEM, FEI Nova NanoSEM 45) equipped with EDX. More structural details were characterized by a field-emission transmission electron microscopy (FETEM, FEI Talos F200X). The surface chemical compositions were studied by X-ray photoelectron spectroscopy (XPS, Shimazduo) using a Kratos Axis Ultra DLD spectrometer. X-ray diffraction (XRD) patterns were measured on a Panalytical X'pert PRO MRD (the Netherlands) with Cu Kα radiation. To perform PDF experiments, the active material was scraped from electrodes and then loaded into a Kapton capillary sealed with glue in an argon-filled glove box. The total scattering experiments were performed by PANalytical Empyrean with Ag Kα radiation and a GaliPIX 3D detector. The raw data were processed using GudrunX [39], and the PDF data are refined using PDFgui [40].

4.3. Electrochemical measurements

The cathode was fabricated by mixing active material with acetylene black and polytetrafluoroethylene in the weight ratio of 7:2:1 using isopropyl alcohol as a wetting agent. Electrochemical tests were performed with CR2032 coin-cells using Zn foil, non-woven fabric, and stainless steel mesh as the anode, separator, and current collector, respectively. A 2-M $Zn(ClO_4)_2$ aqueous solution was employed as the electrolyte. The cells were assembled in an argon-filled glove box. Cyclic voltammograms and electrochemical impedance spectra were measured on Parstat MC 500 (AMETEK). Galvanostatic charge–discharge data were recorded on a BT-2043 Arbin Battery Testing System.

Declaration of competing interest

All the authors declare no conflict of interest.

Acknowledgments

This work was supported by the National Key R&D Program of China (Grant Nos. 2016YFB010030X and 2016YFB0700600) and National Natural Science Foundation of China (Grant Nos. 51772117, 51632001 and 51732005). The authors also thank the Analytical and Testing Centre of HUST for SEM, XRD, XPS, TEM, and other measurements.

Appendix A. Supplementary data

Supplementary data to this article can be found online at https://doi.org/10.1016/j.nanoen.2019.104211.

References

[1] Z.G. Yang, J.L. Zhang, M.C.W. Kintner-Meyer, X.C. Lu, D.W. Choi, J.P. Lemmon, J. Liu, Chem. Rev. 111 (5) (2011) 3577–3613.
[2] B. Dunn, H. Kamath, J.M. Tarascon, Science 334 (6058) (2011) 928–935.
[3] M.S. Whittingham, Chem. Rev. 104 (10) (2004) 4271–4301.
[4] J.B. Goodenough, A. Manthiram, MRS Commun. 4 (4) (2014) 135–142.
[5] D. Larcher, J.M. Tarascon, Nat. Chem. 7 (1) (2015) 19–29.
[6] J.O.G. Posada, A.J.R. Rennie, S.P. Villar, V.L. Martins, J. Marinaccio, A. Barnes, C. F. Glover, D.A. Worsley, P.J. Hall, Renew. Sustain. Energy Rev. 68 (2017) 1174–1182.
[7] D. Kundu, B.D. Adams, V.D. Ort, S.H. Vajargah, L.F. Nazar, Nat. Energy 1 (2016).
[8] G.Z. Fang, J. Zhou, A.Q. Pan, S.Q. Liang, ACS Energy Lett. 3 (10) (2018) 2480–2501.
[9] J.F. Parker, C.N. Chervin, I.R. Pala, M. Machler, M.F. Burz, J.W. Long, D.R. Rolison, Science 356 (6336) (2017) 414–417.
[10] L.Y. Zhang, L. Chen, X.F. Zhou, Z.P. Liu, Adv. Energy Mater. 5 (2) (2015).
[11] K. Lu, B. Song, J.T. Zhang, H.Y. Ma, J. Power Sources 321 (2016) 257–263.
[12] H.L. Pan, Y.Y. Shao, P.F. Yan, Y.W. Cheng, K.S. Han, Z.M. Nie, C.M. Wang, J. H. Yang, X.L. Li, P. Bhattacharya, K.T. Mueller, J. Liu, Nat. Energy 1 (2016).
[13] M. Chamoun, W.R. Brant, C.W. Tai, G. Karlsson, D. Noreus, Energy Storage Mater. 15 (2018) 351–360.
[14] P. He, M.Y. Yan, G.B. Zhang, R.M. Sun, L.N. Chen, Q.Y. An, L.Q. Mai, Adv. Energy Mater. 7 (11) (2017).
[15] X. Guo, G.Z. Fang, W.Y. Zhang, J. Zhou, L.T. Shan, L.B. Wang, C. Wang, T.Q. Lin, Y. Tang, S.Q. Liang, Adv. Energy Mater. 8 (27) (2018).
[16] F. Zhang, M.S. Whittingham, Electrochem. Commun. 2 (1) (2000) 69–71.
[17] C.F. Liu, Z. Neale, J.Q. Zheng, X.X. Jia, J.J. Huang, M.Y. Yan, M. Tian, M.S. Wang, J.H. Yang, G.Z. Cao, Energy Environ. Sci. 12 (7) (2019) 2273–2285.
[18] Y.Q. Yang, Y. Tang, G.Z. Fang, L.T. Shan, J.S. Guo, W.Y. Zhang, C. Wang, L. B. Wang, J. Zhou, S.Q. Liang, Energy Environ. Sci. 11 (11) (2018) 3157–3162.
[19] F. Wan, L.L. Zhang, X. Dai, X.Y. Wang, Z.Q. Niu, J. Chen, Nat. Commun. 9 (2018).
[20] C. Xia, J. Guo, P. Li, X.X. Zhang, H.N. Alshareef, Angew. Chem. Int. Ed. 57 (15) (2018) 3943–3948.
[21] J.W. Ding, Z.G. Du, L.Q. Gu, B. Li, L.Z. Wang, S.W. Wang, Y.J. Gong, S.B. Yang, Adv. Mater. 30 (26) (2018).
[22] F. Wang, E.Y. Hu, W. Sun, T. Gao, X. Ji, X.L. Fan, F.D. Han, X.Q. Yang, K. Xu, C. S. Wang, Energy Environ. Sci. 11 (11) (2018) 3168–3175.
[23] C. Xia, J. Guo, Y.J. Lei, H.F. Liang, C. Zhao, H.N. Alshareef, Adv. Mater. 30 (5) (2018).
[24] N. Zhang, F.Y. Cheng, Y.C. Liu, Q. Zhao, K.X. Lei, C.C. Chen, X.S. Liu, J. Chen, J. Am. Chem. Soc. 138 (39) (2016) 12894–12901.
[25] W. Tang, Y.Y. Hou, F.X. Wang, L.L. Liu, Y.P. Wu, K. Zhu, Nano Lett. 13 (5) (2013) 2036–2040.
[26] O. Tchernyshyov, Phys. Rev. Lett. 93 (15) (2004).
[27] M. Reehuis, A. Krimmel, N. Buttgen, A. Loidl, A. Prokofiev, Eur. Phys. J. B 35 (3) (2003) 311–316.
[28] T. Maitra, R. Valenti, Phys. Rev. Lett. 99 (12) (2007).
[29] Y.Y. Hu, Z.G. Liu, K.W. Nam, O.J. Borkiewicz, J. Cheng, X. Hua, M.T. Dunstan, X. Q. Yu, K.M. Wiaderek, L.S. Du, K.W. Chapman, P.J. Chupas, X.Q. Yang, C.P. Grey, Nat. Mater. 12 (12) (2013) 1130–1136.
[30] K.M.O. Jensen, M. Christensen, P. Juhas, C. Tyrsted, E.D. Bojesen, N. Lock, S.J. L. Billinge, B.B. Iversen, J. Am. Chem. Soc. 134 (15) (2012) 6785–6792.
[31] B.T. Liu, X.M. Shi, X.Y. Lang, L. Gu, Z. Wen, M. Zhao, Q. Jiang, Nat. Commun. 9 (2018).
[32] J. Wang, J. Polleux, J. Lim, B. Dunn, J. Phys. Chem. C 111 (40) (2007) 14925–14931.
[33] V. Augustyn, J. Come, M.A. Lowe, J.W. Kim, P.L. Taberna, S.H. Tolbert, H. D. Abruna, P. Simon, B. Dunn, Nat. Mater. 12 (6) (2013) 518–522.
[34] C. Wu, S.C. Gu, Q.H. Zhang, Y. Bai, M. Li, Y.F. Yuan, H.L. Wang, X.Y. Liu, Y. X. Yuan, N. Zhu, F. Wu, H. Li, L. Gu, J. Lu, Nat. Commun. 10 (2019).
[35] T. Proffen, K.L. Page, S.E. McLain, B. Clausen, T.W. Darling, J.A. TenCate, S.Y. Lee, E. Ustundag, Z. Kristallogr. 220 (12) (2005) 1002–1008.
[36] T. Proffen, S.J.L. Billinge, T. Egami, D. Louca, Z. Kristallogr. 218 (2) (2003) 132–143.
[37] K.W. Chapman, MRS Bull. 41 (3) (2016) 231–238.
[38] B. Shyam, K.W. Chapman, M. Balasubramanian, R.J. Klingler, G. Srajer, P. J. Chupas, Angew. Chem. Int. Ed. 51 (20) (2012) 4852–4855.
[39] A.K. Soper, Science; Council, T. F., GudrunN and GudrunX: Programs for Correcting Raw Neutron and X-Ray Diffraction Data to Differential Scattering Cross Section, Science & Technology Facilities Council, 2011.
[40] C.L. Farrow, P. Juhas, J.W. Liu, D. Bryndin, E.S. Bozin, J. Bloch, T. Proffen, S.J. L. Billinge, J. Phys. Condens. Matter 19 (33) (2007).